

<https://doi.org/10.1038/s42004-025-01582-3>

Kinetic modelling and reactivity of liquid nitromethane under detonation conditions



Teng Zhang¹, Lang Chen¹✉, Kun Yang¹, Bin Zhang¹, Tuo Yang¹, Yao Long², Jianying Lu¹, Danyang Liu¹✉ & Jun Chen^{2,3}✉

Liquid nitromethane (NM) may undergo detonation under accidental stimuli, making kinetic modeling crucial for assessing the safety risks associated with its detonation. This study employs first-principles molecular dynamics to investigate chemical behavior of nitromethane under high temperature (>2000 K) and pressure (>1 GPa) conditions, revealing five previously unidentified intermediates ($\text{CH}_3\text{NO}_2\text{H}$, $\text{CH}_2\text{NO}_2\text{H}$, CH_2NOH , CH_2ONO_2 , NOCH_2NO_2) and establishing a nitromethane chemical kinetic model which include 543 elementary reactions and 79 species, which is successfully applied in the prediction of nitromethane detonation characteristics. The calculated detonation pressure (13.5 GPa) and reaction zone time (46 ns) are in agreement with the experimental values (11.5–12.0 GPa; 50–53 ns). We also uncover the delayed response mechanism in pure nitromethane detonation. The major pollutants, many CO (34.8%), and small amount of NH_3 (1.7%), HCN (1.0%), etc. in nitromethane detonation products are found. These findings advance the fundamental understanding of nitromethane's detonation reaction kinetics.

Nitromethane (NM) is a widely applied liquid homogeneous fuel, explosive and solvent. Recently, NM has gradually attracted widespread interest as an alternative or hybrid fuel for internal combustion engines (ICE)¹. Meanwhile, NM is also produced in bulk quantities for use as a solvent². However, in the process of transportation and storage, under unexpected stimulation, NM could undergo pyrolysis, combustion, and even detonation^{3,4}, which causes serious safety and environmental pollution problems. So far, most studies on the chemical kinetics of NM mainly focus on its pyrolysis and combustion^{5,6}. The study on the detonation chemical kinetics of NM is still very limited, and there is no chemical kinetic model that can be used to predict the detonation performance of NM. In the experiment, only partial detonation characteristic parameters of explosives can be measured, such as detonation pressure and detonation reaction zone time, etc.⁷. Still, it is difficult to directly observe the chemical reaction process in the detonation reaction zone and the composition of detonation products. It is also impossible to evaluate the environmental pollution and human health threats caused by toxic and harmful gases in detonation products.

At present, people have developed many chemical kinetic models of NM, which are mainly widely used to calculate the pyrolysis and combustion reactions of NM^{8–12}. In 1989, Melius et al.⁸ constructed a chemical kinetic model of NM and used it to predict the pyrolysis reaction of NM. The

temperature and chemical species concentration profile with time and the reaction path are obtained and analyzed. In 2015, Brequigny et al.⁹ developed a more detailed chemical kinetic model to calculate the laminar flame speed and species concentration of NM combustion, and verified the accuracy of the model by comparing it with experiments. In 2019, Shrestha et al.^{10,11} further updated the existing model to include a complete formation mechanism for NO_x pollutants. By comparing with the experiment, their model achieves the prediction of species concentration in NM pyrolysis and combustion, and especially improves the ability to predict the emission of polluting gases in NM pyrolysis and combustion. With the continuous development of the chemical kinetic model of NM, the predictive ability and the scope of application of the model are always improving. However, so far, no chemical kinetic model has been reported that can predict the detonation performance and detonation product composition of NM.

The free energy minimization method is the one most commonly used to predict NM detonation properties and detonation product composition. Some well-known detonation performance calculation software, such as Cheetah¹³ and EXPLO5¹⁴, are mainly based on the free energy minimization method to calculate the detonation performance and detonation product composition of various explosives. But these detonation calculation software do not include detailed chemical reaction mechanisms. Although the

¹Beijing Institute of Technology, Beijing, China. ²Laboratory of Computational Physics, Institute of Applied Physics and Computational Mathematics, Beijing, China. ³HEDPS, Center for Applied Physics and Technology, and College of Engineering, Peking University, Beijing, China.

✉e-mail: chenlang@bit.edu.cn; liudy@bit.edu.cn; jun_chen@iapcm.ac.cn

detonation characteristic parameters, such as detonation pressure, detonation temperature and detonation velocity calculated by using different databases or different versions of software are similar, the calculated composition of detonation products is quite different¹⁵. Therefore, this method cannot achieve accurate prediction of detonation product composition. The successful application of the NM chemical kinetic model in predicting the pollutant emissions in NM pyrolysis and combustion^{10,11} means that developing a chemical kinetic model on NM detonation, it is also possible to accurately calculate the detonation chemical reactions of NM and predict its detonation performance as well as the pollutant emissions from detonation products.

In this paper, the chemical kinetics of the pyrolysis of NM under high temperature (>2000 K) and pressure (>1 GPa) is studied by using the first-principles molecular dynamics combined with the quantum chemistry calculation method, the intermediates and elementary reactions are analyzed in detail. Five unreported species—CH₃NO₂H, CH₂NO₂H, CH₂NOH, CH₂ONO₂, and NOCH₂NO₂—are identified, none of which exist in current state-of-the-art kinetic models. Additionally, 24 previously unreported elementary reactions are discovered. These five species are formed via newly identified bimolecular reactions, which play a critical role in the early-stage chemistry of NM under detonation conditions. Based on the species and elementary reactions found in the NM pyrolysis simulations, a NM chemical kinetic model containing 79 species and 543 elementary reactions is constructed. Under experimental conditions, the NM chemical kinetic model is employed to simulate the NM pyrolysis, demonstrating acceptable prediction of species concentration distributions. The same model is further applied to calculate the NM detonation reaction for obtaining the detonation pressure, temperature, reaction zone time and product composition. To verify the calculation result, the interface particle velocity is experimentally measured, obtaining the detonation pressure and reaction zone time. The accuracy and applicability of the NM chemical kinetic model in describing the NM detonation reaction are verified by comparing the calculated values with the experimental values and other theoretical calculation values. We also reveal the composition of detonation products, of which CO is the main polluting gas. This study offers novel insights into the reaction mechanisms of NM under extreme conditions and establishes a predictive framework for evaluating detonation performance and pollutant emissions, advancing the assessment of explosive performance and environmental impact.

Results and discussion

First-principles molecular dynamics simulation of high-density NM pyrolysis

The NM with the density of 2.0 g cm⁻³ pyrolysis under three initial temperatures are simulated. The results show that the main final products are

CO₂, N₂, H₂O, HNCO and NH₃, of which the H₂O is the most abundant. The main intermediates are CH_xNO_y, CH_xONO_y, CH_xNO_yH and CH_xN type molecules and NO₂, NO, OH, CH₂O, CO, etc., small molecules. By using the cluster analysis technique, the number of main intermediates and final products, temperature and pressure at each timestep in pyrolysis can be obtained. By comparing the pyrolysis of NM at different initial temperatures, it is found that the reaction of NM at different temperatures, and the compositions of intermediates and final products are similar. The main difference is that the time at which the reaction reaches equilibrium varies. The higher the temperature, the faster the reaction can reach the final equilibrium state.

To compare the pyrolysis process of NM with different densities, the pyrolysis of NM with the density of 1.1 g cm⁻³ at 2000 K is also simulated. The final products of NM pyrolysis are mainly CO₂, N₂, H₂O and CO. Among them, CO and H₂O are the most abundant. The final product of the pyrolysis of NM with the density of 1.1 g cm⁻³ has more CO and less CO₂ than that of NM with the density of 2.0 g cm⁻³. This indicates that the lower the density, the more CO and the less CO₂ is generated. However, the reaction paths at low density and high density are similar, and it is mainly the frequency of the reaction that is different.

In the following, the pyrolysis of NM with the density of 2.0 g cm⁻³ at an initial temperature of 2000 K is taken as an example to analyze the chemical reaction process. The pyrolysis process of NM with the density of 2.0 g cm⁻³ at initial temperatures of 1600 K, and 2400 K, and the pyrolysis process of NM with the density of 1.1 g cm⁻³ at initial temperatures of 2000 K are shown in Figs. S1, S2 and S3 of Supplementary Information 1.

Figure 1a shows the time evolution of temperature and pressure in NM pyrolysis. Both temperature and pressure began to rise at 10 ps. Until 20 ps, and both reach equilibrium. In the equilibrium state, the temperature and pressure are about 3900 K and 22.5 GPa, respectively. The increased temperature indicates that the overall reaction process of NM is exothermic, while the increased pressure indicates that many small molecular gas products are formed during the reaction.

Figure 1b shows the time evolution of the number of the reactant CH₃NO₂ and final products CO₂, N₂, H₂O, HNCO and NH₃. For CH₃NO₂, at 0–7 ps, its number decreases slowly. At 7–14 ps, its number decreases rapidly. At 14 ps, its number has closed to 0. The decrease in its number is attributed to the unimolecular dissociations and bimolecular reactions of CH₃NO₂.

For H₂O, it appears at 10 ps. At 10–15 ps, its number increases rapidly and reaches equilibrium. While for CO₂, N₂, HNCO and NH₃, they appear and increase after 12 ps. Until 25 ps, their number basically remains constant. Among final products, the H₂O is the most abundant. This is due to the number of H atoms in CH₃NO₂ being the most abundant, while the number of C atoms and N atoms is relatively low.

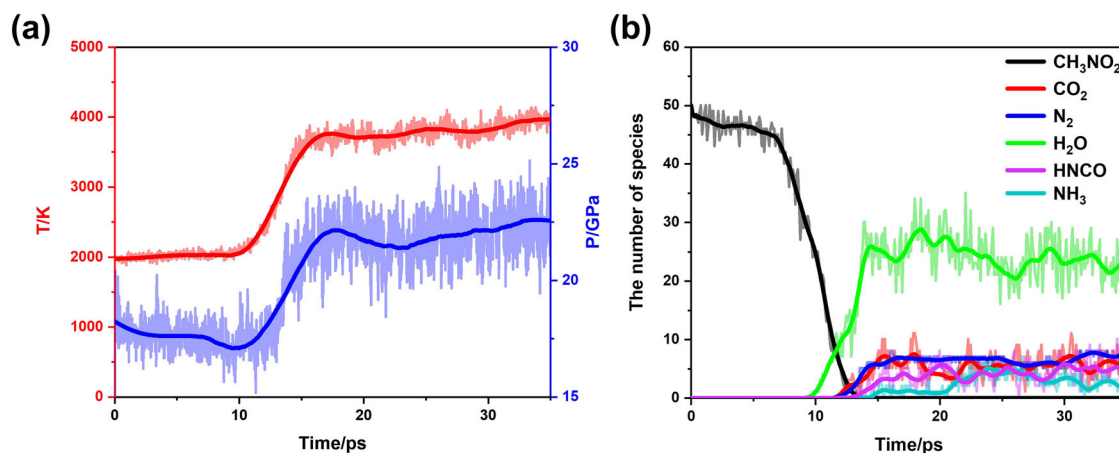


Fig. 1 | Time evolution of temperature, pressure and the number of chemical species in pyrolysis of NM with the density of 2.0 g cm⁻³ at 2000 K. a Temperature and pressure. **b** Reactant and final product. The smooth solid line represents the fitted curve, while the lighter-colored polyline denotes the raw data.

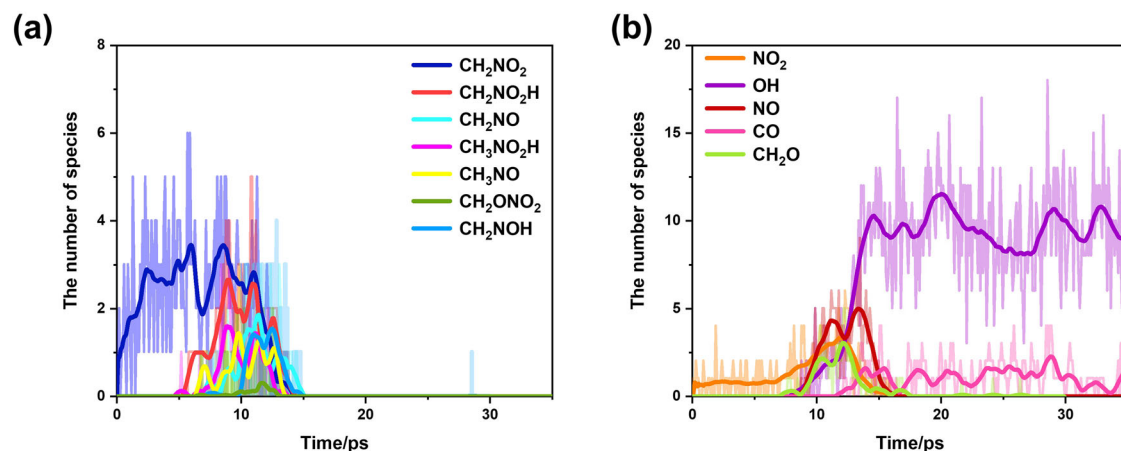


Fig. 2 | Time evolution of the number of intermediates in pyrolysis of NM with the density of 2.0 g cm^{-3} at 2000 K. a CH_xNO_y -, CH_xONO_y - and $\text{CH}_x\text{NO}_y\text{H}$ -type intermediates. **b** Other small molecular intermediates. The smooth solid line represents the fitted curve, while the lighter-colored polyline denotes the raw data.

When the CH_3NO_2 is consumed in large numbers, many intermediates appear. In addition to the small molecules, NO_2 , NO , OH , CO and CH_2O , some molecules containing $-\text{CH}_3$, $-\text{CH}_2$ and $-\text{CH}_2\text{O}$ groups are also observed. Here, in terms of the molecular structures and formulas of these intermediates, these intermediates can be divided into three types, namely CH_xNO_y , CH_xONO_y and $\text{CH}_x\text{NO}_y\text{H}$ ($X=2$ or 3 ; $Y=1$ or 2). The CH_xNO_y -type include CH_3NO , CH_2NO and CH_2NO_2 ; the CH_xONO_y -type include CH_2ONO_2 ; the $\text{CH}_x\text{NO}_y\text{H}$ -type include $\text{CH}_3\text{NO}_2\text{H}$, $\text{CH}_2\text{NO}_2\text{H}$ and CH_2NOH . Among them, the CH_2ONO_2 , $\text{CH}_3\text{NO}_2\text{H}$, $\text{CH}_2\text{NO}_2\text{H}$ and CH_2NOH are not included in the existing state-of-the-art model. According to the elementary analysis, the formation of these species is related to the bimolecular reaction between CH_xNO_y (including CH_3NO_2). In the following, the number distributions of these intermediates are analyzed.

Figure 2a shows the time evolution of the number of intermediates, CH_3NO , CH_2NO , CH_2NO_2 , CH_2ONO_2 , $\text{CH}_3\text{NO}_2\text{H}$, $\text{CH}_2\text{NO}_2\text{H}$ and CH_2NOH . Among them, the CH_2NO_2 first appears at the early NM pyrolysis. Other intermediates appear after 5 ps. But the number of these intermediates is relatively low, they are consumed completely after 15 ps. However, in later analysis, these intermediates play key roles in the early reaction of NM under high temperature and pressure.

Figure 2b shows the time evolution of the number of intermediates, NO_2 , OH , NO , CO and CH_2O . Among them, the NO_2 is the first intermediate. At 0.0–12.5 ps, its number gradually increases and reaches a peak. At 12.5–15.0 ps, its number decreases to 0. The formation of NO_2 is attributed to the unimolecular dissociation of CH_3NO_2 ($\text{CH}_3\text{NO}_2 \rightleftharpoons \text{CH}_3 + \text{NO}_2$). While the OH , NO and CH_2O appear after 7.5 ps. At 7.5–15.0 ps, the number of NO and CH_2O increases first and decreases to 0, while the number of OH increases first and remains constant. The CO appears after 12.0 ps. Its number is always low in the pyrolysis of NM with a density of 2.0 g cm^{-3} . This indicates that the CO is hard to form in the pyrolysis of NM under compressed density. On the contrary, the CO is easier to form under 1.1 g cm^{-3} of theoretical density (as seen in Fig. S3 of Supplementary Information 1). That may mean that the higher CO emissions with NM expansion from maximum compressed density to CJ density in NM detonation.

In the elementary reaction analysis and reaction snapshot observation, unreported 24 elementary reactions and five species are found. Of which, the main formation and consumption paths of these five species have been found, and are shown in Fig. 3. The species marked in blue are these unreported five species. These formations of species are mainly related to the CH_3NO_2 , CH_2NO_2 and CH_2NO . Obviously, these unreported reaction paths are focused on the early reaction stage. After these species are consumed, the subsequent reaction process is similar to the existing model.

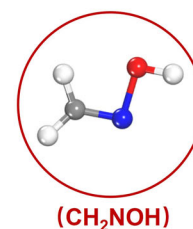
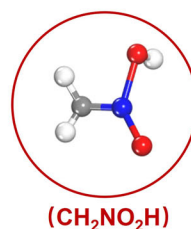
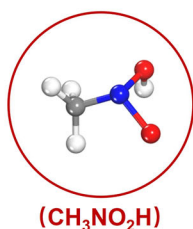
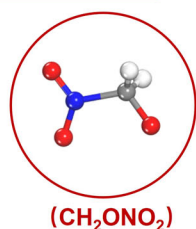
For analyzing the chemical kinetics of these 24 elementary reactions, the quantum chemistry method is adopted to calculate the reaction potential energy surfaces and obtain the Arrhenius rate parameters. In addition, the Arrhenius rate parameters of unimolecular dissociation of CH_3NO_2 , $\text{CH}_3\text{NO}_2 \rightleftharpoons \text{CH}_3 + \text{NO}_2$, under high pressure limit is also calculated for modifying the rate of this reaction under high pressure. This is due to the Arrhenius rate parameters of $\text{CH}_3\text{NO}_2 \rightleftharpoons \text{CH}_3 + \text{NO}_2$ in the existing model are mainly suitable to describe the combustion and pyrolysis under atmospheric pressure⁹ while it can not accurately describe the reaction under high pressure. To facilitate analysis, the reaction can be divided into three types, the first is H-abstraction, the second is O-addition and the third is unimolecular dissociation. These elementary reactions make large contributions to NM pyrolysis under high pressure.

Figure 4 shows the main reaction path and potential energy surfaces of the high-density NM pyrolysis reactions. The purple numbers represent the Gibbs free energy barrier calculated under the B3LYP-D3BJ/Def2-TZVP level at the 298 K, and the red numbers represent the Gibbs free energy barrier calculated under the higher precision CCSD(T)/Def2-TZVP level at the 298 K. By comparison, the Gibbs free energy barrier calculated by CCSD(T)/Def2-TZVP level is significantly higher than that calculated by B3LYP-D3BJ/Def2-TZVP level. The Gibbs free energy barrier calculated by CCSD(T)/Def2-TZVP level is used to analyze chemical reaction kinetics. The remaining reaction and potential energy surface information is displayed in Figs. S4, S5 and S6 of Supplementary Information 1.

Figure 4a shows the potential energy surfaces of the four main H-abstraction reactions. The other six reactions are provided in Fig. S4 of Supplementary Information 1. These H-abstraction reactions can form the intermediates containing the $-\text{OH}$ group, such as identified intermediates, $\text{CH}_3\text{NO}_2\text{H}$, $\text{CH}_2\text{NO}_2\text{H}$ and CH_2NOH . The main reactions are $\text{CH}_3\text{NO}_2 + \text{CH}_3\text{NO}_2 \rightleftharpoons \text{CH}_3\text{NO}_2\text{H} + \text{CH}_2\text{NO}_2$, $\text{CH}_3\text{NO}_2 + \text{CH}_2\text{NO}_2 \rightleftharpoons \text{CH}_2\text{NO}_2 + \text{CH}_2\text{NO}_2\text{H}$, $\text{CH}_3\text{NO}_2 + \text{CH}_3\text{NO} \rightleftharpoons \text{CH}_2\text{NO}_2\text{H} + \text{CH}_2\text{NO}$ and $\text{CH}_3\text{NO}_2 + \text{CH}_2\text{NO} \rightleftharpoons \text{CH}_2\text{NO}_2 + \text{CH}_2\text{NOH}$. Among these H-abstraction reactions, the bimolecular reaction of $\text{CH}_3\text{NO}_2 + \text{CH}_3\text{NO}_2 \rightleftharpoons \text{CH}_3\text{NO}_2\text{H} + \text{CH}_2\text{NO}_2$ has the highest free energy barrier of $302.83 \text{ kJ mol}^{-1}$. This suggests that the reaction is kinetically inhibited at low temperatures. Furthermore, as a bimolecular process, its occurrence becomes more favorable under elevated temperatures and increased CH_3NO_2 concentrations. Some H-abstraction reactions will form the irritant gas HCOOH , which is related to OCHO . The HCO and CH_2O can also form HCOOH . These reactions have also been revealed in the oxidation of CH_4 and C_2H_2 ^{16,17}. But the importance of $\text{CH}_3\text{NO}_2\text{H}$, $\text{CH}_2\text{NO}_2\text{H}$ and CH_2NOH still needs to be analyzed in detail.

Figure 4b shows the potential energy surfaces of the four main O-addition reactions. The other six reactions are provided in Fig. S5 of Supplementary Information 1. In these O-addition reactions, many

Molecular snapshot



Reaction pathway

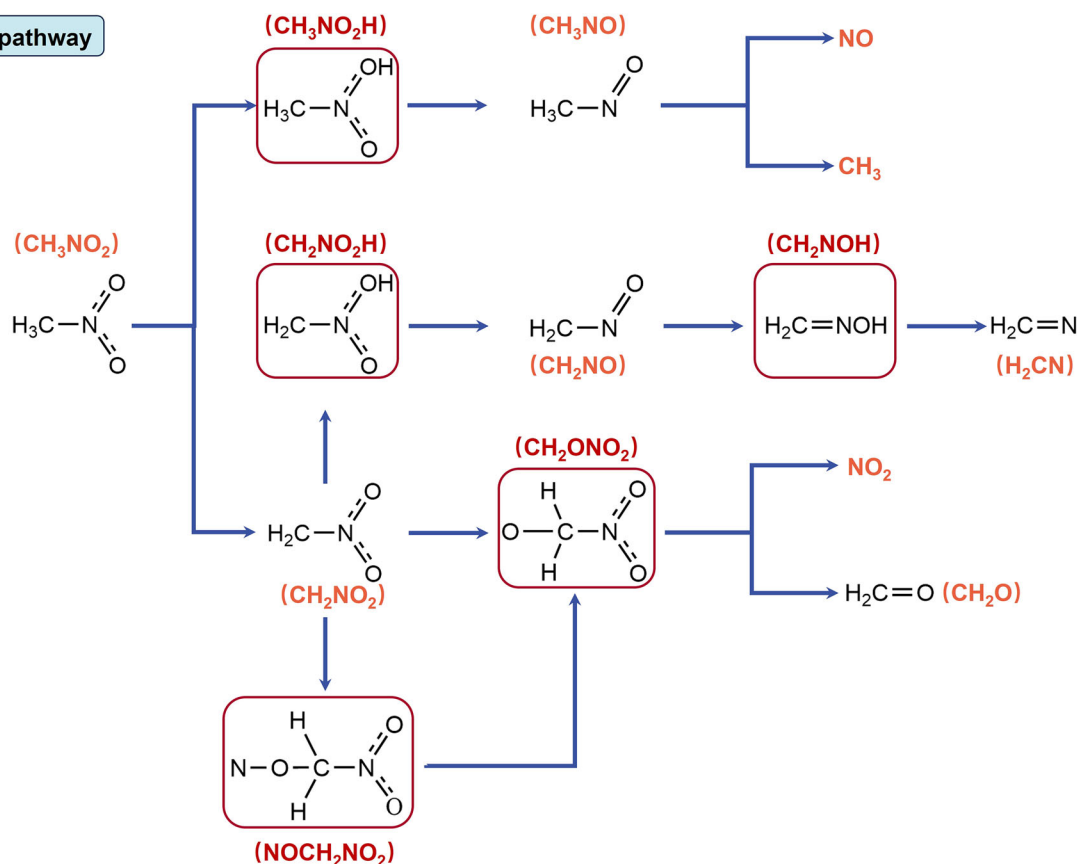


Fig. 3 | The main formation and consumption paths of five newfound species.

O-containing species are formed. Of which, the main formation reactions of CH_2ONO_2 and NOCH_2NO_2 are $\text{CH}_3\text{NO}_2 + \text{CH}_2\text{NO}_2 \rightarrow \text{CH}_2\text{ONO}_2 + \text{CH}_3\text{NO}$, $\text{NOCH}_2\text{NO}_2 + \text{NO} \rightarrow \text{CH}_2\text{ONO}_2 + \text{N}_2\text{O}$ and so on.

The formation of CH_2ONO_2 has a low Gibbs free energy barrier and is exothermic, while the formation of NOCH_2NO_2 is mainly endothermic. In addition, in some O-addition reactions, no stable intermediate is formed, but after O-addition, the molecule is directly decomposed into CH_2O , such as the reaction $\text{CH}_3\text{NO}_2 + \text{CH}_2\text{NO} \rightarrow \text{CH}_3\text{NO} + \text{NO} + \text{CH}_2\text{O}$. These O-addition reactions mainly oxidize the C atom. Among the 10 O-addition reactions, 8 reactions are exothermic. This indicates most O-addition reactions are thermodynamically favorable.

Figure 4c shows the potential energy surfaces of the four main unimolecular dissociation reactions. Another reaction is provided in Fig. S6 of Supplementary Information 1. These reactions include the dissociations of four intermediates, CH_2ONO_2 , $\text{CH}_3\text{NO}_2\text{H}$, $\text{CH}_2\text{NO}_2\text{H}$, and CH_2NOH . In these dissociation reactions, active radicals will be formed, such as OH and NO_2 . In terms of potential energy surface, four reactions, $\text{CH}_3\text{NO}_2\text{H} \rightarrow \text{CH}_3\text{NO} + \text{OH}$, $\text{CH}_2\text{NO}_2\text{H} \rightarrow \text{CH}_2\text{NO} + \text{OH}$ and $\text{CH}_2\text{NOH} \rightarrow \text{H}_2\text{CN} + \text{OH}$ are endothermic, one reaction, $\text{CH}_2\text{ONO}_2 \rightarrow$

$\text{CH}_2\text{O} + \text{NO}_2$ is exothermic. In terms of the potential energy surface, the $\text{CH}_2\text{ONO}_2 \rightarrow \text{CH}_2\text{O} + \text{NO}_2$ is a reaction with zero energy barrier. Therefore, the reaction is easier to occur and is important to the formation of pollution gases.

Based on the potential energy surface, the Arrhenius rate parameters of unreported 24 elementary reactions and unimolecular dissociation of CH_3NO_2 are calculated under the level of CCSD(T)/Def2-TZVP. Table 1 shows the Arrhenius rate parameters of these 25 elementary reactions.

The initial dissociation reaction ($\text{CH}_3\text{NO}_2 \rightleftharpoons \text{CH}_3 + \text{NO}_2$) is a key reaction, and some researchers have determined its rate constant through both computational and experimental approaches. We also compared the rate constants we calculated with those in the literature, such as the result of Zhu et al.¹⁸ and Brequigny et al.⁹ But there are differences between our calculated rate constant at high pressure limit and their obtained rate constant, as shown in Fig. S7 of Supplementary Information 1.

This is mainly because this rate constant of Brequigny et al. is obtained by fitting the experimental data¹⁹ within 2000 K and under near-normal pressure conditions, while this rate constants of Zhu et al. and others are calculated based on the dissociation energy, which is different from these

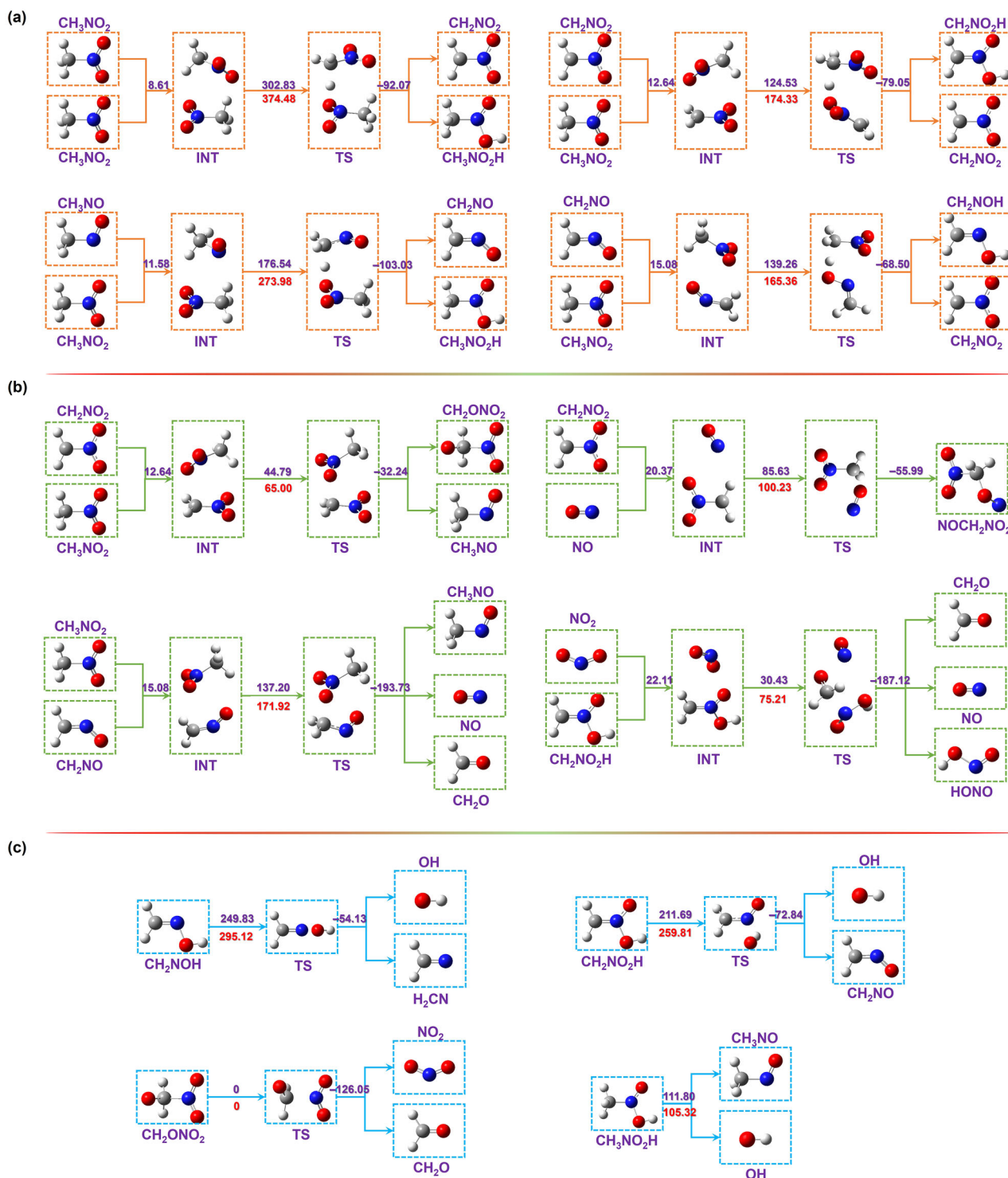


Fig. 4 | The main reactions and their potential energy surface. a H-abstraction reactions, (b) O-addition reactions, (c) Unimolecular dissociation. The purple number refers to the $\Delta G(298\text{ K})$ in the level of B3LYP-D3BJ/Def2-TZVP, the red number refers to the $\Delta G(298\text{ K})$ in the level of CCSD(T)/Def2-TZVP. Note that the

$\Delta G(298\text{ K})$ of CCSD(T)/Def2-TZVP corresponds to the high-precision electronic energy from CCSD(T)/Def2-TZVP plus the thermal correction to Gibbs free energy from B3LYP-D3BJ/Def2-TZVP. When the calculated energy barrier is a negative value, it is regarded as a zero energy barrier and is marked as 0 in the figure.

ways of calculating the reaction rate constant at high pressure limit using the Gibbs free energy barrier in this paper.

The NM pyrolysis and detonation simulation based on model

Based on the obtained elementary reactions and chemical species in the NM pyrolysis simulation, combined with the quantum chemistry method and rate parameters of the other model, a detailed chemical kinetics model of

NM is constructed, namely the FP-NM model. The FP-NM model contains 79 species and 543 elementary reactions, and it will be used to calculate the pyrolysis at near-atmospheric pressure and detonation.

In this paper, the NM pyrolysis is performed in PSR and PFR to obtain the species concentration profile with temperature. NM detonation reaction is calculated in shock tube reactor for obtaining the species concentration, pressure and temperature with time. In the following, the calculated value

Table 1 | The Arrhenius rate parameter of 25 elementary reactions

Reaction	Arrhenius rate parameter				Method
	<i>A</i>	<i>m</i>	<i>E_a</i>		
$\text{CH}_3\text{NO}_2 \rightleftharpoons \text{CH}_3 + \text{NO}_2$	$3.3 \times 10^7 (1.8 \times 10^{16})^a$	3.1 (0.0) ^a	95804.1 (58500) ^a		TS
$\text{CH}_2\text{ONO}_2 \rightleftharpoons \text{CH}_2\text{O} + \text{NO}_2$	1.2×10^{11}	0.8	8754.8		VTST
$\text{CH}_3\text{NO}_2 + \text{CH}_3\text{NO}_2 \rightleftharpoons \text{CH}_3\text{NO}_2\text{H} + \text{CH}_2\text{NO}_2$	1.16×10^{11}	0.7	88370.4		TS
$\text{CH}_3\text{NO}_2 + \text{CH}_3\text{NO} \rightleftharpoons \text{CH}_3\text{NO}_2\text{H} + \text{CH}_2\text{NO}$	8.13×10^9	0.2	62344.1		TS
$\text{CH}_3\text{NO}_2 + \text{CH}_2\text{NO}_2 \rightleftharpoons \text{CH}_3\text{NO} + \text{CH}_2\text{ONO}_2$	1.02×10^{12}	−0.3	13479.1		TS
$\text{CH}_3\text{NO}_2 + \text{CH}_2\text{ONO}_2 \rightleftharpoons \text{HCO} + \text{NO}_2 + \text{CH}_3\text{NO}_2\text{H}$	9.78×10^{10}	1	78671.4		TS
$\text{HONO} + \text{OCHO} \rightleftharpoons \text{NO}_2 + \text{HCOOH}$	1.95×10^2	2.2	−15801.7		VTST
$\text{CH}_3\text{NO}_2 + \text{OCHO} \rightleftharpoons \text{CH}_2\text{NO}_2 + \text{HCOOH}$	9.67×10^{10}	0.2	13964.2		TS
$\text{CH}_3\text{NO}_2 + \text{CH}_2\text{NO}_2 \rightleftharpoons \text{CH}_2\text{NO}_2\text{H} + \text{CH}_2\text{NO}_2$	3.89×10^{10}	0.2	39491		TS
$\text{CH}_2\text{NO}_2\text{H} + \text{NO}_2 \rightleftharpoons \text{NO} + \text{CH}_2\text{O} + \text{HONO}$	2.78×10^{10}	0.2	15316.6		TS
$\text{CH}_2\text{NO}_2\text{H} + \text{N}_2\text{O} \rightleftharpoons \text{N}_2 + \text{CH}_2\text{O} + \text{HONO}$	2.80×10^{10}	−0.2	72920		TS
$\text{CH}_3\text{NO}_2 + \text{CH}_2\text{NO} \rightleftharpoons \text{CH}_2\text{NOH} + \text{CH}_2\text{NO}_2$	4.03×10^{10}	0.3	37665.5		TS
$\text{CH}_2\text{NO} + \text{OCHO} \rightleftharpoons \text{HCNO} + \text{HCOOH}$	3.16×10^9	0.5	8857.8		TS
$\text{CH}_3\text{NO}_2\text{H} \rightleftharpoons \text{CH}_3\text{NO} + \text{OH}$	1.85×10^{12}	2.6	34031.1		TS
$\text{CH}_3\text{NO}_2 + \text{CH}_2\text{NO} \rightleftharpoons \text{CH}_3\text{NO} + \text{NO} + \text{CH}_2\text{O}$	1.55×10^{11}	−0.4	37665.5		TS
$\text{CH}_2\text{NO}_2 + \text{NO} \rightleftharpoons \text{CH}_2\text{NO} + \text{NO}_2$	2.55×10^{10}	−0.1	36814.8		TS
$\text{CH}_2\text{NOH} + \text{CH}_3 \rightleftharpoons \text{CH}_3\text{OH} + \text{H}_2\text{CN}$	5.76×10^9	0.7	26755.1		TS
$\text{CH}_2\text{NO} + \text{H}_2\text{CN} \rightleftharpoons \text{HCN} + \text{CH}_2\text{NOH}$	1.64×10^{10}	0.2	51507.8		TS
$\text{CH}_2\text{NO} + \text{NO}_2 \rightleftharpoons \text{HCNO} + \text{HONO}$	2.21×10^{12}	−0.5	49256.9		TS
$\text{CH}_2\text{NO}_2 + \text{NO} \rightleftharpoons \text{NOCH}_2\text{NO}_2$	2.48×10^{10}	−0.1	20308.2		TS
$\text{NOCH}_2\text{NO}_2 + \text{NO} \rightleftharpoons \text{N}_2\text{O} + \text{CH}_2\text{ONO}_2$	6.76×10^{11}	0.5	3983.3		TS
$\text{CH}_2\text{NO}_2\text{H} \rightleftharpoons \text{CH}_2\text{NO} + \text{OH}$	8.57×10^{10}	1.1	63154.1		TS
$\text{CH}_2\text{NO}_2 + \text{HCO} \rightleftharpoons \text{OCHO} + \text{CH}_2\text{NO}$	5.05×10^{11}	−0.3	20236.6		TS
$\text{NO}_2 + \text{HCO} \rightleftharpoons \text{OCHO} + \text{NO}$	6.10×10^{11}	−0.5	20341.7		TS
$\text{CH}_2\text{NOH} \rightleftharpoons \text{H}_2\text{CN} + \text{OH}$	1.06×10^{11}	1.1	71553.2		TS

^a The rate parameter of reaction $\text{CH}_3\text{NO}_2 \rightleftharpoons \text{CH}_3 + \text{NO}_2$ at atmospheric pressure is derived from Brequigny's model⁹.

will be compared with the experimental value, the result will be analyzed in detail.

Figure 5a, b shows the calculated value and experimental value of species concentration profile with temperature in NM pyrolysis in PSR (pyrolysis experiment in JSR, calculation in PSR). The experimental value derives from the result of Yang et al.²⁰ The initial calculation condition is the same as the experimental condition. The molar fraction of CH_3NO_2 is 1.00%, the molar fraction of bath gas Ar is 99.00%, the temperature range is 675–1225 K, the pressure is 1 atm. Figure 5d also shows the calculated value and experimental value of species concentration profile with temperature in NM pyrolysis in PSR. The experimental value derives from the result of Shrestha et al.¹¹ The initial calculation condition is the same as the experimental condition. The molar fraction of CH_3NO_2 is 1.00%, the molar fraction of bath gas He is 99.00% (here the bath gas He is replaced by bath gas Ar), the temperature range is 500–1100 K, the pressure is 1.07 bar. Figure 5e, f shows the calculated value and experimental value of species concentration profile with temperature in NM pyrolysis in PFR. The experimental value derives from the result of Shrestha et al.¹¹ The initial calculation condition is the same as the experimental condition. The molar fraction of CH_3NO_2 is 1.00%, the molar fraction of bath gas He is 99.00% (here the bath gas He is replaced by bath gas Ar), the temperature range is 500–1100 K, the pressure is 1.07 bar. In Fig. 5, the predicted molar fraction of most species has good agreement with the experimental value. However, the consistency between the calculated values and the experimental values shows differences within different temperature ranges. When the temperature is below 1000 K, the predicted value is closer to experimental value, when the temperature is above 1000 K, the predicted precision is relatively

low. But in general, the model-predicted value matches well with experimental value, the FP-NM model can basically describe the pyrolysis kinetics of NM.

Here, we also analyzed the chemical kinetic causes of these differences between the calculated value and the experimental value. According to the ROP analysis (Fig. S8 of Supplementary Information 1), we have found the main reaction that results in the deviation of calculated and experimental species concentration of Fig. 5a and 7b at above 1000 K. For CO, the main reaction is $\text{HCO} + \text{NO} \rightleftharpoons \text{HNO} + \text{CO}$. For H_2 , the main reaction is $\text{OH} + \text{H}_2 \rightleftharpoons \text{H} + \text{H}_2\text{O}$. For CH_4 , the main reactions are $\text{CH}_3 + \text{HNO} \rightleftharpoons \text{NO} + \text{CH}_4$ and $\text{CH}_4 + \text{OH} \rightleftharpoons \text{CH}_3 + \text{H}_2\text{O}$. For C_2H_6 , the main reaction is $\text{CH}_3 + \text{CH}_3 (+\text{M}) \rightleftharpoons \text{C}_2\text{H}_6 (+\text{M})$. More detailed analysis can be seen in Fig. S8 of Supplementary Information 1.

While in Fig. 5e, the reason for the discrepancies between calculated and experimental H_2O and CO concentrations is different from the above-mentioned. The key factor is intermediate, HCOOH (Fig. S9 of Supplementary Information 1). The formation path of HCOOH will compete with that of CO and H_2O for HCO and OH. More detailed analysis can be seen in Fig. S9 of Supplementary Information 1. Building upon the above analysis, we emphasize the necessity of giving special consideration to these reactions and related kinetics when refining the kinetic model.

Although some researchers have developed many chemical kinetics models on NM pyrolysis and combustion^{8–10,12}, these models cannot describe the NM detonation. Our FP-NM model not only can describe the reaction in NM pyrolysis, but also can describe the reaction in NM detonation. In the following, the FP-NM model will be used to predict the NM detonation performance and pollution gas emissions. To verify the FP-NM

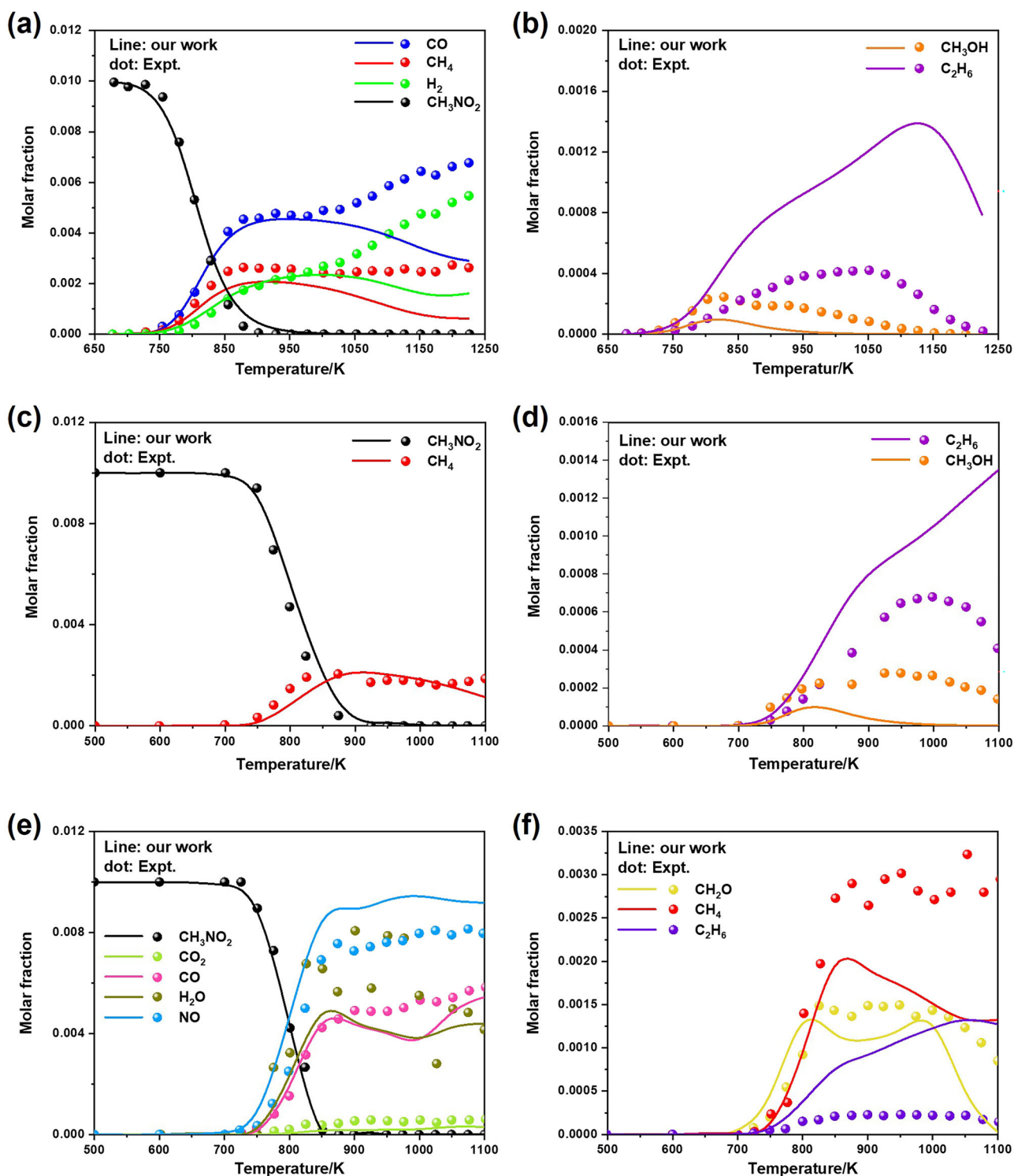


Fig. 5 | The predicted and experimental species molar fractions for nitromethane pyrolysis. a, b The NM pyrolysis in PSR. The experimental data from Yang et al.²⁰. **c, d** The NM pyrolysis in PSR. The experimental data from Shrestha et al.¹¹ **e, f** The

NM pyrolysis in PFR. The experimental data from Shrestha et al.¹¹ The resident time in PSR and PFR reactor is all 2.0 s.

model's accuracy, the laser interferometry method is adopted to measure the interface particle velocity (u_p) and CJ detonation velocity (D_{CJ}) in NM detonation. According conversion relationship between interfacial particle velocity and pressure²¹, the CJ detonation pressure (P_{CJ}) and reaction zone time (τ_{CJ}) can be obtained. Then the FP-NM model is used to calculate the NM detonation reaction after shock in the Shock Tube Reactor, and predict

the CJ detonation pressure (P_{CJ}), temperature (T_{CJ}) and reaction zone time (τ_{CJ}). According to the NM reaction calculation under shock by Reed et al.²², the pressure and temperature can reach about 25 GPa and 2000 K after shock, respectively. Therefore, the temperature and pressure after shock are set as 25 GPa and 2000 K, respectively. Finally, the calculated value will be compared with the experimental value.

In this paper, two sets of particle velocity measurement experiments are carried out. Figure 6 shows the experimentally interface particle velocity curves of NM/LiF for two sets of experiments. The CJ point is approximately determined based on the inflection point in particle velocity profiles, yielding measured reaction zone time of 50 ns and 53 ns for the two parallel experiments. The measured detonation velocities (D_{CJ}) are 6110 and 6120 m s⁻¹, respectively. Then, according to the conversion equation²¹, the detonation pressures (P_{CJ}) are obtained as 12.0 and 11.5 GPa, respectively.

Figure 7a, b shows the species molar fraction profile and temperature, and pressure profile with time, respectively. In terms of species molar fraction profile, at about 46 ns, the chemical species basically reach chemical and thermodynamic equilibrium, so this point is identified as the CJ point. The reaction zone time (τ_{CJ}) is 46 ns. In terms of temperature and pressure profile, at about 46 ns, the detonation pressure (P_{CJ}), temperature (T_{CJ}) are 3985 K and 13.5 GPa, respectively. Of which, the predicted reaction zone time (τ_{CJ}) and detonation pressure (P_{CJ}) match well with the above experimentally measured values. In the calculated pressure and temperature profile, an interesting phenomenon can be found a slow change zone of 6 ns before the profile changes rapidly. In the experimental measurement of Sheffield et al.⁷, they have found that the particle velocity curve of pure liquid NM has a slow change zone of about 4 ns before a rapid decline, which is close to the results of our calculation. According to the analysis, in Fig. 7a,

within the slow change zone of 6 ns, the CH₃NO₂ has been consumed to about 30%. This indicates that the early reaction is slow and the gas emissions are relatively less, which induces the pressure and temperature change slowly. Therefore, the initial reactant consumption rate determines the delayed response time of pure NM.

Furthermore, several detonation characteristic quantities obtained by calculation and experiment in this paper are compared with the existing detonation calculation software Cheetah and the experimental results of other researchers^{7,15,23–30}, as shown in Table 2. The experimental and calculated P_{CJ} , T_{CJ} , τ_{CJ} and D_{CJ} obtained in this paper are in good agreement with most of the experimental and calculated results. This also means that our FP-NM model has good accuracy in predicting the NM explosive detonation performance.

However, due to the composition of detonation products, it cannot be accurately measured in detonation experiments, so only the calculated results of the FP-NM model are presented and compared with the calculation results of Cheetah¹⁵. The mass fraction of the main detonation product calculated by the FP-NM model and the mass fraction of the main detonation product calculated by Cheetah based on three different combinations of equations of state & databases are presented in Table 2. According to the calculation results in Table 2, NM of 1.000 g will produce CO of 0.348 g, NH₃ of 0.017 g, CH₂O of 0.003 g, HCOOH of 0.003 g and HCN of 0.010 g. It can be seen that the detonation product mass fraction calculated by the FP-NM model is close to the result calculated by Cheetah based on Jcz3&SNL, but is quite different from those calculated by Cheetah based on BKW&LLNL and BKW&SNL. Specifically, compared with the calculation result of the FP-NM model, H₂O formation is overestimated and CO formation is underestimated in the calculation by Cheetah based on BKW&LLNL. However, CO₂ formation is overestimated and CO formation is underestimated in the calculation by Cheetah based on BKW&SNL. Only the mass fractions of N₂ obtained by these methods are relatively close, while the mass fractions of the calculated detonation products are mainly different in CO₂, CO and H₂O.

The above analysis shows that there is always a deviation between the results of the FP-NM model and those of Cheetah in terms of detonation product composition. This is mainly because the chemical reaction process is not considered in the calculation of Cheetah, and there are still large uncertainties in the prediction of detonation product composition. Therefore, the free energy minimization method cannot achieve an accurate prediction of detonation product composition. In contrast, the FP-NM model considers a variety of chemical species and chemical reaction processes. In addition, the FP-NM model can already accurately predict the concentration distribution of each species in the NM thermal decomposition. Therefore, the FP-NM model for the prediction of the composition of detonation products will be more accurate.

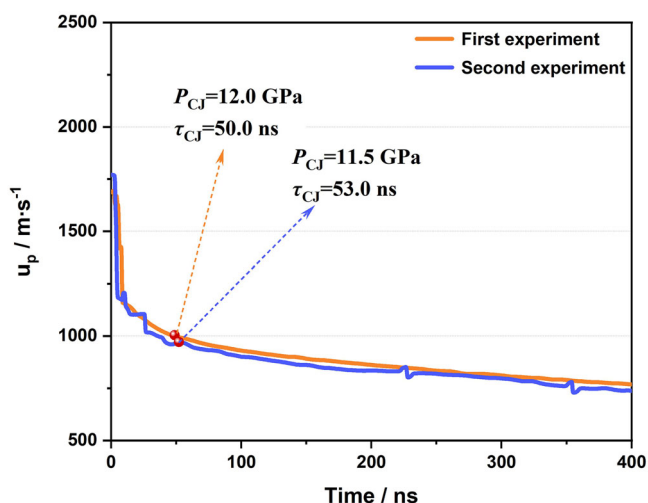


Fig. 6 | The experimental particle velocity profile at the interface of NM/LiF. These are two sets of parallel experiments.

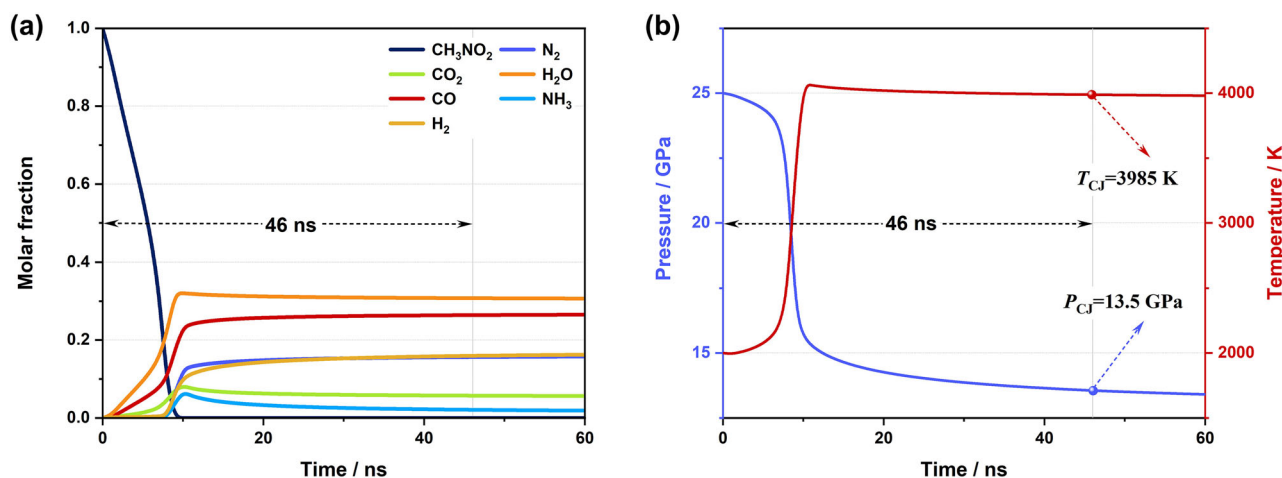


Fig. 7 | The calculated temperature, pressure and species concentration profile by using FP-NM model. a Species concentration. b Temperature and pressure.

Table 2 | The calculated and experimental value of CJ detonation characteristic quantity

CJ detonation characteristic quantity	Cal. in this work	Expt. in this work	Cheetah BKW&LLNL data	Cheetah BKW&SNL data	Cheetah JCZ3&SNL data	Expt. from other studies
P_{CJ}/GPa	13.5	12.0, 11.5	11.4 ^a	13.2 ^a	11.7 ^a	12.6–13.1 ^b , 12.5 ^c , 13.0 ^d , 12.6 ^e
T_{CJ}/K	3985	–	3666 ^a	3626 ^a	3442 ^a	3430 ^f
τ_{CJ}/ns	46	50, 53	–	–	–	50 ^{g,h} , 6 ⁱ , 100–150 ^j
$D_{CJ}/\text{km s}^{-1}$	–	6.12, 6.11	–	–	–	6.18–6.34 ^b , 6.30 ^{c,d} , 6.28 ^{e,g}
$g(\text{H}_2\text{O})/g(\text{NM})$	0.259	–	0.412 ^a	0.190 ^a	0.253 ^a	–
$g(\text{CO})/g(\text{NM})$	0.348	–	0.164 ^a	0.032 ^a	0.247 ^a	–
$g(\text{CO}_2)/g(\text{NM})$	0.116	–	0.087 ^a	0.402 ^a	0.183 ^a	–
$g(\text{N}_2)/g(\text{NM})$	0.207	–	0.229 ^a	0.256 ^a	0.210 ^a	–
$g(\text{H}_2)/g(\text{NM})$	0.015	–	–	0.003 ^a	0.008 ^a	–
$g(\text{NH}_3)/g(\text{NM})$	0.017	–	–	0.025 ^a	0.023 ^a	–
$g(\text{HCOOH})/g(\text{NM})$	0.003	–	–	0.056 ^a	0.031 ^a	–
$g(\text{CH}_2\text{O})/g(\text{NM})$	0.003	–	–	–	–	–
$g(\text{HCN})/g(\text{NM})$	0.010	–	–	–	–	–

a Ref. 15; b Ref. 24; c Ref. 25; d Ref. 26; e Ref. 23; f Ref. 27; g Ref. 7; h Ref. 28; i Ref. 29; j Ref. 30. BKW&LLNL data represent BKW equation of state and Los Alamos National Laboratory data base. BKW&SNL data represent BKW equation of state and Sandia National Laboratory data base. JCZ3&SNL data represent JCZ3 equation of state and Sandia National Laboratory data base.

^aRef. 15.

^bRef. 24.

^cRef. 25.

^dRef. 26.

^eRef. 23.

^fRef. 27.

^gRef. 7.

^hRef. 28.

ⁱRef. 29.

^jRef. 30.

In the NM detonation, the FP-NM model can not only calculate the characteristic parameters of NM detonation, but also predict the composition of NM detonation products, so as to obtain the emission of polluting gases caused by NM detonation. According to the calculation results in Table 2, among all of the polluting gases, the mass fraction of CO is the largest. This indicates that CO is the most harmful pollutant gas to human health and the environment in NM detonation. Through reaction path analysis and species generation rate analysis, it is found that CO formation mainly depends on a chain reaction process, which can be expressed as: $\text{CH}_2\text{ONO}_2/\text{CH}_2\text{OH}/\text{CH}_3\text{O} \rightarrow \text{CH}_2\text{O} \rightarrow \text{HCO} \rightarrow \text{CO}$. In this chain reaction, CH_2ONO_2 , as a newly identified species, is also important for CO formation.

Accurate prediction of detonation chemical reactions using FP-NM models depends on an accurate reaction mechanism. Compared with other chemical kinetics models, the chemical species and elementary reactions in the FP-NM model are obtained based on first-principles molecular dynamics simulations. And FP-NM model contains newly identified five species and 24 reactions, of which four species ($\text{CH}_3\text{NO}_2\text{H}$, $\text{CH}_2\text{NO}_2\text{H}$, CH_2ONO_2 , CH_2NOH) and related reactions have a large contribution to the NM detonation reaction process. By calculating the ROP in the NM detonation reaction, the ROP profile of $\text{CH}_3\text{NO}_2\text{H}$, $\text{CH}_2\text{NO}_2\text{H}$, CH_2ONO_2 and CH_2NOH can be obtained, as shown in Fig. 8. A positive ROP value means that the species is formed, and a negative ROP value means that the species is consumed.

Figure 8a shows the ROP profile of $\text{CH}_3\text{NO}_2\text{H}$ with time. Two reactions play key roles in the formation and consumption of $\text{CH}_3\text{NO}_2\text{H}$. Specifically, $\text{CH}_3\text{NO}_2 + \text{CH}_3\text{NO}_2 = > \text{CH}_3\text{NO}_2\text{H} + \text{CH}_2\text{NO}_2$ is important to the formation of $\text{CH}_3\text{NO}_2\text{H}$, this reaction is also one of the initial reactions. While $\text{CH}_3\text{NO}_2\text{H} = > \text{CH}_3\text{NO} + \text{OH}$ has an important contribution to the consumption of $\text{CH}_3\text{NO}_2\text{H}$. This indicates that the $\text{CH}_3\text{NO}_2\text{H}$ is mainly decomposed into OH radical.

Figure 8b shows the ROP profile of $\text{CH}_2\text{NO}_2\text{H}$ with time. Two reactions play key roles in the formation and consumption of $\text{CH}_2\text{NO}_2\text{H}$.

Specifically, $\text{CH}_3\text{NO}_2 + \text{CH}_2\text{NO}_2 = > \text{CH}_2\text{NO}_2\text{H} + \text{CH}_2\text{NO}_2$ has a large contribution to the formation of $\text{CH}_2\text{NO}_2\text{H}$, while $\text{CH}_2\text{NO}_2\text{H} = > \text{CH}_2\text{NO} + \text{OH}$ has a large contribution to the consumption of $\text{CH}_2\text{NO}_2\text{H}$, and it is also mainly decomposed into OH radical.

Figure 8c shows the ROP profile of CH_2ONO_2 with time. Two reactions play key roles in the formation and consumption of CH_2ONO_2 . Specifically, $\text{CH}_3\text{NO}_2 + \text{CH}_2\text{NO}_2 = > \text{CH}_3\text{NO} + \text{CH}_2\text{ONO}_2$ contributes to the formation of CH_2ONO_2 . While $\text{CH}_2\text{ONO}_2 = > \text{CH}_2\text{O} + \text{NO}_2$ plays a key role in the consumption of CH_2ONO_2 , it is decomposed into pollution gases, CH_2O and NO_2 .

Figure 8d shows the ROP profile of CH_2NOH with time. Two reactions play key roles in the formation and consumption of CH_2NOH . Specifically, $\text{CH}_3\text{NO}_2 + \text{CH}_2\text{NO} = > \text{CH}_2\text{NOH} + \text{CH}_2\text{NO}_2$ contributes to the formation of CH_2NOH . While $\text{CH}_2\text{NOH} = > \text{H}_2\text{CN} + \text{OH}$ contributes to the consumption of CH_2NOH , forming OH radical.

According to the ROP analysis of these four species, $\text{CH}_3\text{NO}_2\text{H}$, $\text{CH}_2\text{NO}_2\text{H}$, CH_2NOH and CH_2ONO_2 are formed by bimolecular reactions which occur before 10 ns. And $\text{CH}_3\text{NO}_2\text{H}$, $\text{CH}_2\text{NO}_2\text{H}$, CH_2ONO_2 and CH_2NOH are mainly decomposed into OH radicals, and CH_2ONO_2 is mainly decomposed into CH_2O and NO_2 in the NM detonation reaction process.

The number of these four species in the detonation reaction is small, which is due to these species will be consumed quickly at the same time of formation. Therefore, in the ROP profile, it can be shown that their formation and consumption are in the same period, and they have a certain contribution to the early reaction of NM detonation. The formation and consumption of these four species are consistent with the results of first-principles molecular dynamics simulations.

Further, the effect of these four species on the detonation reaction of NM is analyzed. Removing both the four species and the related reactions from the FP-NM model and then calculating the NM detonation reaction process. Figure 9 is a comparison of the pressure curves calculated by the FP-NM model and the FP-NM model without these four species. In Fig. 9, the

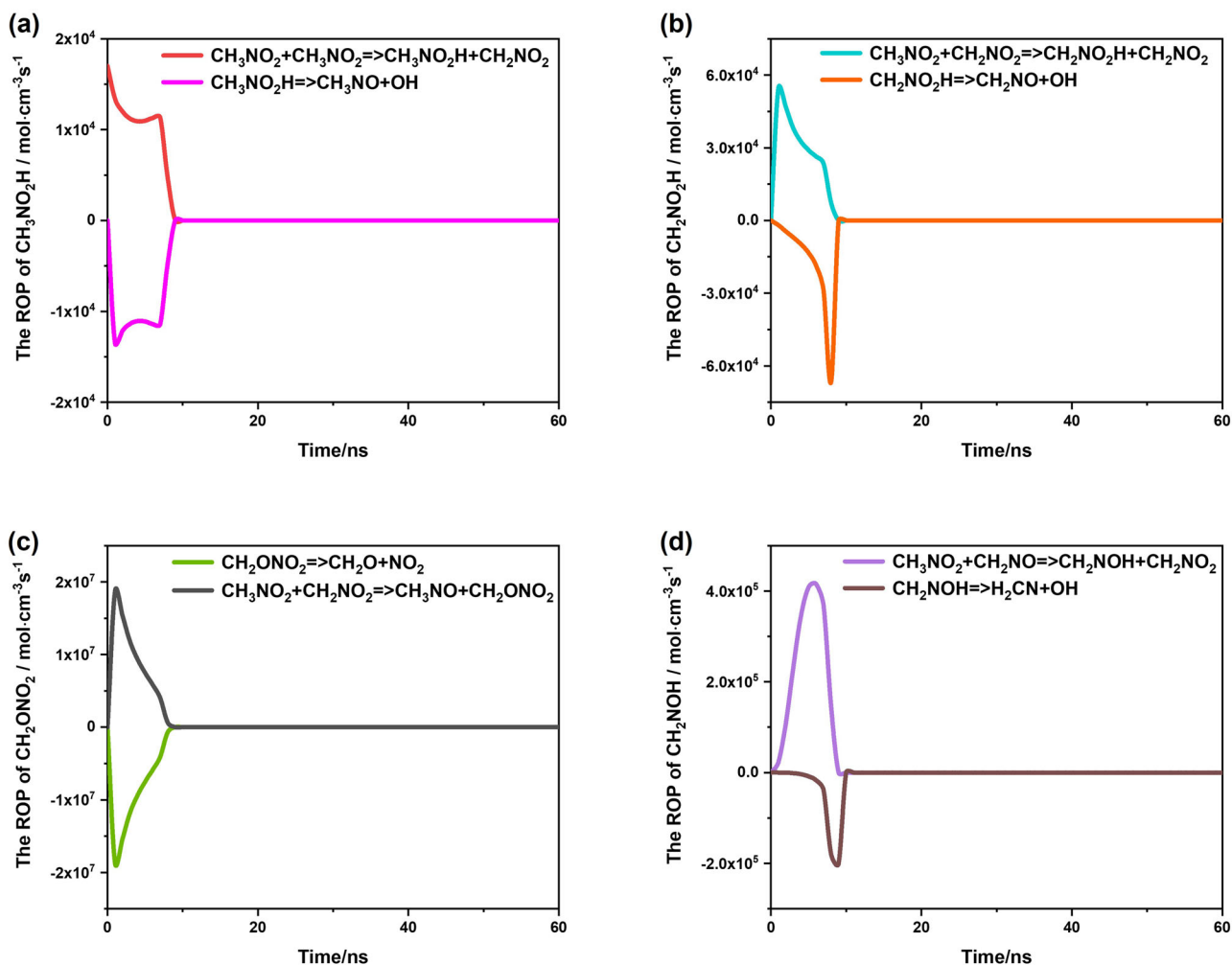


Fig. 8 | The calculated ROP for four newfound species on NM detonation reaction. (a) CH₃NO₂H, (b) CH₂NO₂H, (c) CH₂ONO₂, (d) CH₂NOH.

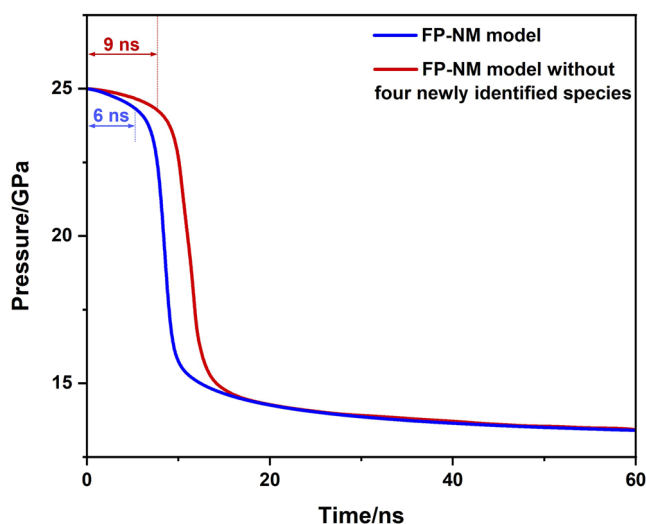


Fig. 9 | Comparison of calculated pressure of the model with/without the four identified species.

pressure calculated by the FP-NM model without these four species needs to go through a slowly changing region of 9 ns, while the pressure calculated by the FP-NM model only needs to go through a slowly changing region of 6 ns. Figure 9 shows the pressure, temperature and species concentration

profile with time in the NM detonation reaction calculated using the FP-NM model without these four species, respectively. But the calculated P_{CJ} and τ_{CJ} by these two models are basically consistent. This indicates that these four species and related reactions mainly affect the early detonation chemical reaction process, and hardly affect the CJ point of the reaction. It is also shown in first-principles molecular dynamics simulation that these species are all formed by bimolecular reactions in the reaction. It follows that bimolecular reactions are important in reactions under high temperature and high pressure conditions, and these bimolecular reactions will accelerate the early chemical reaction of detonation, thereby affecting the rate of change of system pressure and temperature with time.

In the experimental particle velocity measurement by Sheffield et al.⁷, it has been found that there is a slow change zone of particle velocity in the early reaction, and the reaction zone time is about 4 ns. Therefore, the slow change zone of 9 ns calculated by the FP-NM model without these four species is significantly too wide and deviates greatly from the experimental measurement. This further indicates that the newly revealed species and reactions play an important role in the early detonation chemical reaction of NM.

Finally, to further analyze the specific influence of the newly identified reactions on the detonation of NM, we calculated the temperature sensitivity coefficients of these reactions in the Closed Homogeneous Reactor under initial conditions of 25 GPa and 2000 K (consistent with the initial temperature and pressure settings used in the detonation reaction calculations for NM). For comparative reference, the temperature sensitivity coefficients of the typical initial reaction ($\text{CH}_3\text{NO}_2 \rightleftharpoons \text{CH}_3 + \text{NO}_2$) are also listed. Figure 10 presents the temperature sensitivity coefficients of both the initial

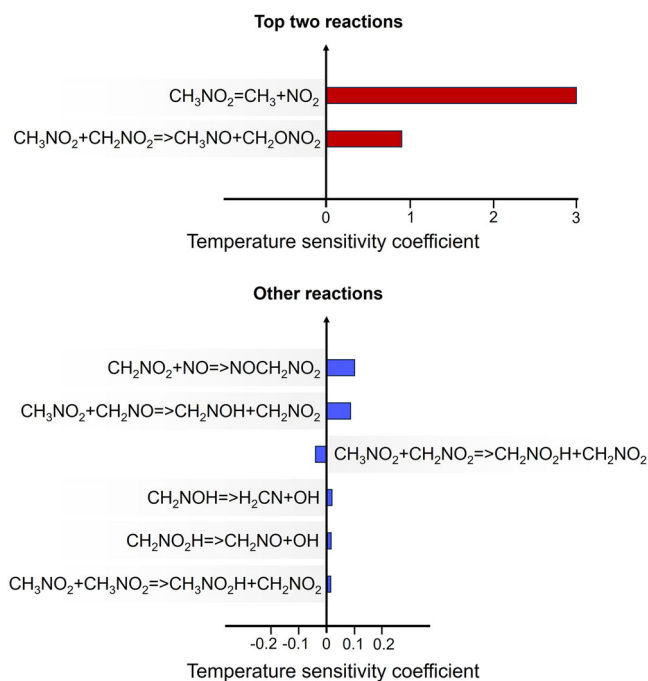


Fig. 10 | The temperature sensitivity coefficient of initial and part of identified reactions.

and newly identified reactions, where a positive value indicates that the reaction promotes heat release, while a negative value signifies an inhibitory effect on heat release. Only reactions with temperature sensitivity coefficients greater than 0.001 are displayed in Fig. 10.

The results reveal that two reactions exhibit notably large positive temperature sensitivity coefficients: one is the initial reaction $\text{CH}_3\text{NO}_2 = \text{CH}_3 + \text{NO}_2$, and the other is the bimolecular reaction $\text{CH}_3\text{NO}_2 + \text{CH}_2\text{NO}_2 = \text{CH}_3\text{NO} + \text{CH}_2\text{ONO}_2$. This indicates that both reactions play a significant role in the detonation of NM. In contrast, the other six reactions show relatively lower temperature sensitivity coefficients compared to these two. Among them, five have positive coefficients, while one exhibits a negative coefficient, suggesting that these six reactions also exert a limited but measurable influence on the detonation reaction kinetics of NM. The above analysis indicates that among all the newly identified reactions, reaction $\text{CH}_3\text{NO}_2 + \text{CH}_2\text{NO}_2 = \text{CH}_3\text{NO} + \text{CH}_2\text{ONO}_2$ contributes the most to the detonation of NM.

Conclusions

In this paper, the pyrolysis of NM under high temperature and pressure is simulated based on the first-principles molecular dynamics method. In combination with quantum chemistry methods, the chemical kinetic model of NM explosives that can accurately calculate pyrolysis and detonation reactions has been developed. The model contains 79 species and 543 elementary reactions. The accuracy and applicability of the model are verified by numerical simulation and experimental comparison. Specific conclusions are as follows:

1. Based on the first-principles molecular dynamics simulation, unreported five species, $\text{CH}_3\text{NO}_2\text{H}$, $\text{CH}_2\text{NO}_2\text{H}$, CH_2NOH , CH_2ONO_2 , NOCH_2NO_2 and 24 reactions are revealed. These species are all formed by bimolecular reactions, which will accelerate the rate of NM in the early detonation reaction, resulting in a faster release of energy.
2. By combining the first-principles molecular dynamics and quantum chemistry methods, we constructed a chemical kinetic model containing 79 species and 543 elementary reactions, and used the model to calculate the pyrolysis and detonation reactions of NM. The mechanism of the delayed response of pure NM in the early stage of detonation is revealed.

3. The CJ detonation reaction zone time, CJ detonation pressure and CJ detonation temperature are successfully predicted by using FP-NM model. The accuracy and applicability of the model are verified by comparing the calculated values of the model with the experimental values and the theoretical values calculated by the detonation parameter calculation software.
4. The composition of CJ detonation products is obtained by calculation by using FP-NM model, among which CO and H_2O are the two most abundant products. The main polluting gases in detonation products are CO, and a small amount of HCN, NH_3 , CH_2O , HCOOH , etc.

This study provides novel insights into the pyrolysis and detonation reaction mechanism of NM, lays a foundation for the construction of chemical kinetic models and performance prediction of explosives, and provides a way for the assessment of air pollution and human health risks caused by the emission of explosive detonation products.

Methods

Computational method

In this paper, NM model construction and reaction performance calculation are mainly performed through three steps. The first step is to obtain the elementary reaction and the chemical species by the first-principles molecular dynamics (FPMD) method. The second step is to obtain the Arrhenius rate parameters of the elementary reaction and the thermodynamic parameters of the chemical species through quantum chemistry calculation. The third step is to integrate the elementary reaction, chemical species, Arrhenius rate parameters and thermodynamic parameters to form Model files, and use the constructed chemical kinetics model to calculate the pyrolysis and detonation performance of the explosive³¹. Figure 11 shows the schematic diagram of the calculation process. The calculation method of each step is shown as follows.

The density functional theory (DFT)-based FPMD method is used to simulate the chemical reaction of HEDMs in the HASEM software package^{16,17,31–35}. The generalized gradient approximation (GGA) is used for the exchange-correlation function in the Perdew–Burke–Ernzerhof (PBE) form. Dynamics are based on the Born–Oppenheimer (BO) approximation. In the BO approximation, the motion of an atom is divided into the motion of the nucleus and the motion of the electrons. The electronic structure is solved by DFT-based quantum chemical calculations. The motion of the atomic nucleus is solved by MD simulations. The combination of DFT calculations based on BO approximation and MD simulations is known as the FPMD (or ab initio MD) method. The van der Waals interaction of the C–H–N–O system is well considered in HASEM by constructing a set of pseudopotentials and pseudoatomic orbital basis specialized for molecular systems consisting of C/H/N/O elements. In the simulation, we used the Perdew–Burke–Ernzerhof (PBE) exchange-correlation function³⁶. The PBE exchange-correlation function used in HASEM has good accuracy in describing the interaction of C–H–N–O complexes, the interaction between some complexes even reaches the accuracy of the CCSD method³³. Meanwhile, the DZP basis set is used, which is a choice made considering the number of atoms (350 atoms) to be simulated to ensure a balance between efficiency and accuracy. The specific step method will be shown below.

The simulation of NM pyrolysis. First, the computational model with the density of 1.1 g cm^{-3} and 2.0 g cm^{-3} is constructed, respectively. Both models contain 50 NM molecules, 350 atoms in total. 1.1 g cm^{-3} corresponds to the density of NM at room temperature, and 2.0 g cm^{-3} corresponds to the maximum compression density of NM after shock^{15,37}.

Then the two computational models are relaxed at 298 K under the NVT ensemble to obtain the stable computational model at room temperature. Further, the stable computational model with the density of 2.0 g cm^{-3} is relaxed at constant temperatures of 1600, 2000, and 2400 K under the NVT ensemble, and the stable computational model with the density of 1.1 g cm^{-3} is relaxed at constant temperatures of 2000 K under the NVT ensemble. The temperature is controlled using a Nosé–Hoover thermostat³⁸ so that the NM basically reaches thermodynamic equilibrium

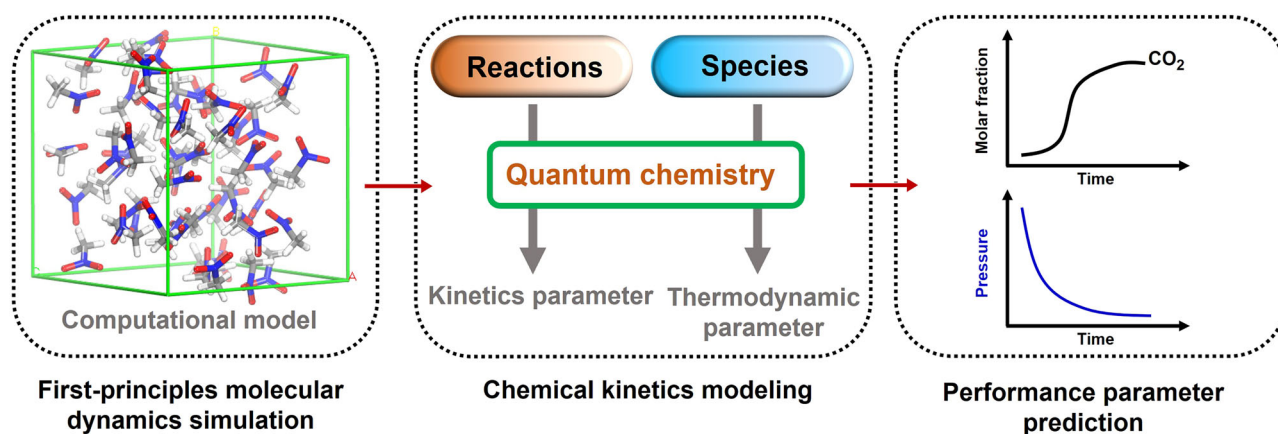


Fig. 11 | Schematic diagram of the research route.

at the set temperature and does not decompose. And this makes sure the temperature at the initial stage of the reaction can be kept stable at a constant temperature to avoid large oscillations in temperature under the NVE ensemble. Finally, the pyrolysis of the NM computational model with the density of 2.0 g cm^{-3} at initial temperatures of 1600, 2000, and 2400 K is simulated under the NVE ensemble, respectively. Meanwhile, the pyrolysis of NM computational model with the density of 1.1 g cm^{-3} at initial temperatures of 2000 K is also simulated under the NVE ensemble.

The cut-off energy set in the simulation is 1000 eV, and the energy convergence criterion is $1.0 \times 10^{-4} \text{ eV}$. The time step and total simulation time are set to 0.2 fs and 20–55 ps, respectively. The initial temperature and simulation time settings are inversely proportional.

In this work, the three-parameter Arrhenius equation is used to describe the reaction rate constant k of an elementary reaction, as follows:

$$k = AT^m e^{-E_a/RT} \quad (1)$$

where A is the pre-exponential factor and m is the temperature coefficient. The E_a is the energy barrier of the elementary reaction. For a bimolecular reaction, the unit of A is $\text{cm}^3 \text{ mol}^{-1} \text{ s}^{-1}$. For an unimolecular reaction, the unit of A is s^{-1} . The unit of E_a is J mol^{-1} .

To get the values of A and m , we calculate the reaction rate constant k at different temperatures according to the Eyring equation

$$k = \frac{k_B T}{h} e^{-\Delta G_f^\ddagger(T)/RT} \quad (2)$$

where the $\Delta G_f^\ddagger(T)$ is Gibbs free energy barrier, the unit is J mol^{-1} ; k_B is Boltzmann's constant ($1.380649 \times 10^{-23} \text{ J K}^{-1}$); h is Planck's constant ($6.62606957 \times 10^{-34} \text{ J s}$); T is temperature and R is gas constant ($8.314 \text{ J mol}^{-1} \text{ K}^{-1}$). Using the fitting technique, combining Eqs. (1) and (2), the parameter A and m can be obtained. The $\Delta G_f^\ddagger(T)$ can be calculated by the following formula:

$$\Delta G_f^\ddagger(T) = G(\text{TS}) - G(\text{reactant}) \quad (3)$$

In this paper, the chemical kinetics parameter is calculated by using the quantum chemical method in Gaussian 16³⁹ and Kisthelp⁴⁰ software. All molecular structures and transition states are optimized under the level of B3LYP-D3BJ/Def2-TZVP, then the thermal correction Gibbs free energy is obtained. The B3LYP functional combined with the Def2-TZVP⁴¹ basis set, is widely applicable to molecules containing C–H–N–O elements⁴². With the incorporation of the D3BJ⁴³ dispersion correction term, it effectively accounts for dispersion interactions, ensuring both accuracy in geometric structure optimization and high computational efficiency. While the high-precision electronic energy is calculated at the level of CCSD(T)/Def2-

TZVP. The CCSD(T) method is universally recognized as the “gold standard” for energy calculations and is typically the preferred choice for obtaining high-accuracy electronic energies. However, due to its low efficiency in geometry optimization and significant memory demands, it is generally unsuitable for molecular structure optimization^{44,45}. Finally, the high-precision Gibbs free energy can be obtained by combining the thermal correction Gibbs free energy of B3LYP-D3BJ/Def2-TZVP level with high-precision electronic energy of CCSD(T)/Def2-TZVP level.

For a reaction satisfying the transition state theory (TST), the reaction rate constant k at different temperatures can be obtained by calculating the Gibbs free energy barrier $\Delta G_f^\ddagger(T)$ at different temperatures in combination with Eq. (2). According to k at different temperatures, Eq. (1) can be fitted to obtain the Arrhenius rate parameter, which refers to the temperature coefficient m of the pre-exponential factor A .

The conventional TST approach is primarily suitable for reactions with high energy barriers. However, when the reaction barrier is relatively low (typically $<5 \text{ kcal mol}^{-1}$), quantum effects (such as tunneling) and zero-point energy corrections become significant, leading to potential underestimation of reaction rates by classical TST. In such cases, the variational transition state theory (VTST) method is employed for more accurate rate constant calculations⁴⁶. The core of VTST is to determine the best transition state on the reaction path by the variational method. Even if the free energy barrier is near zero, VTST can still accurately describe the reaction path and kinetics. For the rate calculation satisfying the VTST, the calculation results obtained in Gaussian 16 are imported into Kisthelp⁴⁰ for Arrhenius rate parameter calculation.

Based on the elementary reaction, the Arrhenius parameters of the elementary reaction, the chemical species and the thermodynamic parameters of species, a detailed chemical kinetic model of NM can be constructed. The thermodynamic parameters of species and the Arrhenius parameters of the reactions are calculated by the quantum chemistry method, while other existing species, elementary reactions and related parameters are directly referred from Brequigny et al.⁹, Gao et al.¹² and the developed FP-CH₄ model¹⁶ by our previous work. In the following discussion, we call the NM detailed chemical kinetic models as FP-NM model.

The FP-NM model is used to calculate the NM pyrolysis and detonation reaction under conditions of the same experiment in Chemkin Pro software⁴⁷ for predicting the performance of NM in pyrolysis and detonation. The Perfectly Stirred Reactor (PSR) and Plug Flow Reactor (PFR) are used to calculate the pyrolysis reaction for obtaining the species concentration profile. The Shock Tube Reactor is used to calculate the detonation reaction of NM for obtaining the CJ detonation pressure (P_{CJ}), temperature (T_{CJ}), reaction zone time (τ_{CJ}), etc., detonation characteristic parameters and detonation product composition. Then these calculation values will be compared with experimental values to verify the accuracy and applicability of the FP-NM model.

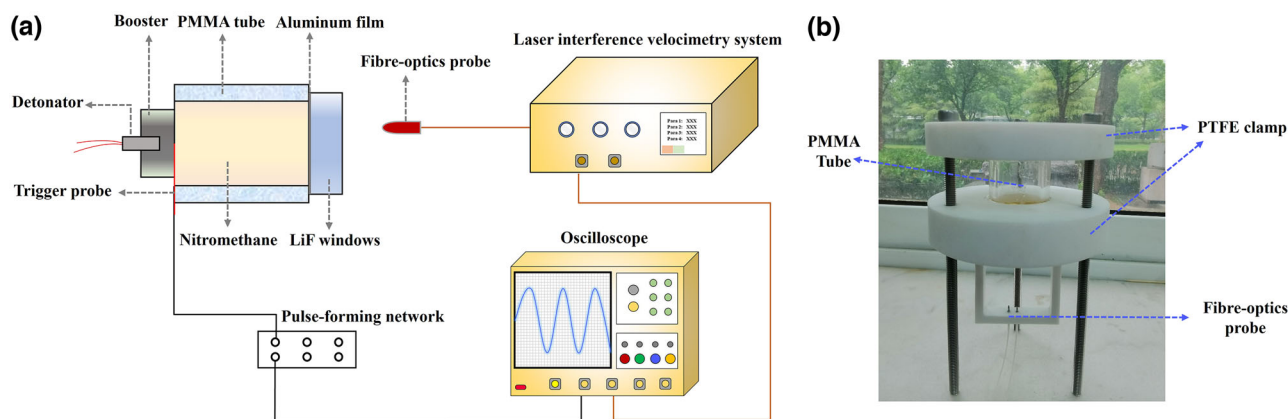


Fig. 12 | The device and test principle of the experiment. a The schematic diagram of the testing system. **b** The photo of the testing device.

Experimental method

In this paper, the interface particle velocity between liquid nitromethane (NM) explosive and window is measured by the laser interferometry method^{21,23}. Figure 12a is the principle of the test system. The test system consists of detonator, loading explosive, liquid nitromethane explosive, trigger probe, LiF transparent window, pulse-forming network, optical fiber probe, all-fiber interferometric velocimetry system and oscilloscope. Liquid nitromethane is placed in a polymethyl methacrylate (PMMA) tube with an inner diameter of 25 mm and a length of 40 mm. The lower end of the PMMA tube is mounted with a LiF window, and the surface of the LiF window in contact with NM is plated with an aluminum film with a thickness of 600 nm. The edges of the LiF window are sealed with epoxy glue to prevent liquid leakage. Two Polytetrafluoroethylene (PTFE) splints and bolts are used to fix the PMMA tube, window as well as the probe holder. Figure 12b shows the photo of the testing device. During the experiment, the detonator initiates the loading explosive, and the explosive is loaded to produce a detonation wave to detonate the NM. A trigger probe is installed between the loading explosive and the NM. When the detonation wave reaches the position of the trigger probe, due to the conductivity of the detonation wave, causing short circuit so that the pulse forms a network to output the pulse signal, and the oscilloscope is triggered to start recording the laser interference signal. Then, the interference signal is transformed to obtain the interface particle velocity between the NM and the window. At the same time, according to the time signal given by the trigger probe (t_0) and the time of interface particle velocity jump (t_1), the propagation time of the detonation wave in NM can be obtained, and the detonation velocity of nitromethane can be estimated by further combining the length of the explosive column.

In the experiment, the loading explosive is an RDX-based explosive (RDX/binder = 95/5). The density of NM is 1.1 g cm^{-3} . The focal length of the fiber probe is 70 mm, and the laser wavelength used in the test is 1550 nm. The oscilloscope simulation bandwidth is 12.5 GHz, the sampling frequency is up to 40 GS s^{-1} , and the recording time interval used in the experiment is 40 ps.

Data availability

The data that support the conclusions of this study are available in the paper and the Supplementary files or from the corresponding author on reasonable request. Additional result, discussion and figure are provided in Supplementary Information 1. The atomic position coordinates of the initial and final states of first-principles molecular dynamics are provided in Supplementary Data 1, the atomic coordinates of optimized molecular structure and transition state are provided in Supplementary Data 2, the Model Files, including kinetics and thermodynamic data, are provided in Supplementary Data 3.

Abbreviation

FPMD	first-principles molecular dynamics
A	pre-exponential factor
NM	nitromethane
m	temperature coefficient
P_{CJ}	CJ detonation pressure
$\Delta G_f^\ddagger(T)$	Gibbs free energy barrier
T_{CJ}	CJ detonation temperature
k	rate constant
τ_{CJ}	detonation reaction zone time
PSR	perfectly stirred reactor
D_{CJ}	CJ detonation velocity
PFR	plug flow reactor
DFT	density functional theory
JFR	jet stirred reactor
TST	transition state theory
RDX	cyclotrimethylenetrinitramine
VTST	variational transition state theory
u_p	particle velocity
E_a	activation energy barrier
CJ	Chapman-Jouguet theory

Received: 28 February 2025; Accepted: 6 June 2025;

Published online: 19 June 2025

References

- Litzinger, T. et al. Fuel additive effects on soot across a suite of laboratory devices, Part 2: Nitroalkanes. *Combust. Sci. Technol.* **183**, 739–754 (2011).
- Liu, J. et al. Nitromethane as a nitrogen donor in Schmidt-type formation of amides and nitriles. *Science* **367**, 281–285 (2020).
- Menikoff, R. & Shaw, M. S. Modeling detonation waves in nitromethane. *Combust. Flame* **158**, 2549–2558 (2011).
- Kurilov, M. et al. Ignition of nitromethane-based propellant mixtures. *Int. J. Energetic Mater. Chem. Propulsion* **23** (2024).
- Yang, M., Wu, Y., Tang, C., Liu, Y. & Huang, Z. Auto-ignition behaviors of nitromethane in diluted oxygen in a rapid compression machine: critical conditions for ignition, ignition delay times measurements, and kinetic modeling interpretation. *J. Hazard. Mater.* **377**, 52–61 (2019).
- Naucélér, J. D., Li, Y., Nilsson, E. J. K., Curran, H. J. & Konnov, A. A. An experimental and modeling study of nitromethane + O₂ + N₂ ignition in a shock tube. *Fuel* **186**, 629–638 (2016).
- Sheffield, S. A. et al. Particle velocity measurements of the reaction zone in nitromethane. In *Proc 12th International Detonation Symposium*. 159–166 (Office of Naval Research, 2002).

8. Melius, C. F. *Thermochemical Modeling: II. Application to Ignition and Combustion of Energetic Materials* (Springer Netherlands, 1990).
9. Brequigny, P. et al. Laminar burning velocities of premixed nitromethane/air flames: An experimental and kinetic modeling study. *Proc. Combust. Inst.* **35**, 703–710 (2015).
10. Shrestha, K. P., Seidel, L., Zeuch, T. & Mauss, F. Kinetic modeling of NO_x formation and consumption during methanol and ethanol oxidation. *Combust. Sci. Technol.* **191**, 1628–1660 (2019).
11. Shrestha, K. P. et al. Insights into nitromethane combustion from detailed kinetic modeling – Pyrolysis experiments in jet-stirred and flow reactors. *Fuel* **261**, 116349 (2020).
12. Gao, Z. et al. Measurements of the high temperature ignition delay times and kinetic modeling study on oxidation of nitromethane. *Combust. Sci. Technol.* **192**, 313–334 (2020).
13. Fried, L. E., Howard, W. M. & Souers, P. C. CHEETAH 2.0 User's Manual. LLNL Report UCRL-MA-117541 (1998).
14. Suceska, M. Calculation of detonation parameters by EXPLO5 computer program. *Mater. Sci. Forum* **325–330** (2004).
15. Štimac, B., Chan, H. Y. S., Kunel, M. & Sućeska, M. Numerical modelling of detonation reaction zone of nitromethane by EXPLO5 code and Wood and Kirkwood theory. *Cent. Eur. J. Energ. Mater.* **17**, 239–261 (2020).
16. Zhang, T. et al. Detailed and reduced chemical kinetic model of CH₄/air mixtures combustion based on high-precision first-principles molecular dynamics simulation. *Chem. Eng. Sci.* **281**, 119159 (2023).
17. Zhang, T. et al. Insight into the high-temperature oxidation kinetics of acetylene: a first-principles molecular dynamics study. *J. Hazard. Mater.* **466**, 133613 (2024).
18. Zhu, R. S., Raghunath, P. & Lin, M. C. Effect of roaming transition states upon product branching in the thermal decomposition of CH₃NO₂. *J. Phys. Chem. A* **117**, 7308–7313 (2013).
19. Glänzer, K. & Troe, J. Thermische zerfallsreaktionen von nitroverbindungen i: Dissoziation von nitromethan. *Helvetica Chim. Acta* **55**, 2884–2893 (1972).
20. Yang, M. et al. Nitromethane pyrolysis and oxidation in a jet-stirred reactor: experimental measurements, kinetic model validation and interpretation. *Fuel* **263**, 116491 (2020).
21. Liu, D., Chen, L., Wang, C. & Wu, J. Detonation reaction characteristics for CL-20 and CL-20-based aluminized mixed explosives. *Cent. Eur. J. Energ. Mater.* **14**, 573–588 (2017).
22. Reed, E., Riad Manaa, M., Fried, L. E., Glaesemann, K. R. & Joannopoulos, J. D. A transient semimetallic layer in detonating nitromethane. *Nat. Phys.* **4**, 72–76 (2008).
23. Štimac, B., Kuenzel, M., Sućeska, M., Stanković, S. & Kucera, J. Detonation reaction zone in nitromethane: experimental and numerical studies. *Seminar on New Trends in Research of Energetic Materials* (2019).
24. Mochalova, V. et al. Reaction zone structure and detonation parameters of nitromethane/polymethylmethacrylate and its mixture with microballoons. *Phys. Fluids* **33**, 046108 (2021).
25. Dobratz, B. M. LLNL Explosives Handbook. DE85-015961 (1981).
26. Utkin, A. V., Mochalova, V. M. & Garanin, V. A. Structure of detonation waves in nitromethane and a nitromethane/methanol mixture. *Combust. Expl. Shock Waves* **48**, 350–355 (2012).
27. Hobbs, M. L. & Bear, M. R. Calibrating the BKW-EOS with a large product Species Data Base and measured C-J properties. In *Proc 10th Int. Detonation Symposium*. 409–418 (Office of Naval Research, 1995).
28. Mochalova, V., Utkin, A. & Lapin, S. Detonation properties of nitromethane/diethylenetriamine solution. *AIP Conf. Proc.* **2017**, 030005 (1973).
29. Engelke, R. & Bdzil, J. B. A study of the steady-state reaction-zone structure of a homogeneous and a heterogeneous explosive. *Phys. Fluids* **26**, 1958–1988 (1983).
30. Bouyer, V. et al. Experimental measurements of the chemical reaction zone of detonating liquid explosives. *AIP Conf. Proc.* **1195**, 177–180 (2009).
31. Zhang, T. et al. Performance prediction of high-energy-density material CL-20 based on FP-CL20 chemical kinetics model. *Combust. Flame* **277**, 114180 (2025).
32. HASEM (V1.3.1). <http://www.caep-scns.ac.cn/HASEM.php>.
33. Zhang, L. et al. Phase transition in octahydro-1,3,5,7-tetra-nitro-1,3,5,7-tetrazocine (HMX) under static compression: an application of first-principles method specialized for CHNO solid explosives. *J. Phys. Chem. B* **120**, 11510–11522 (2016).
34. Zhang, L. et al. Stabilization of the dual-aromatic cyclo-N5-anion by acidic entrapment. *J. Phys. Chem. Lett.* **10**, 2378–2385 (2019).
35. Zhang, T., Xia, W., Fan, W., Chen, L. & Chen, J. Oxidation kinetic mechanism of n-decane under high temperature and pressure: a first-principles molecular dynamics study. *Phys. Chem. Chem. Phys.* **25**, 32471 (2023).
36. Perdew, J. P., Burke, K. & Ernzerhof, M. Generalized gradient approximation made simple. *Phys. Rev. Lett.* **77**, 3865–3868 (1996).
37. Partom, Y. Revisiting shock initiation modeling of homogeneous explosives. *J. Energ. Mater.* **31**, 127–142 (2013).
38. Nose, S. A unified formulation of the constant temperature molecular dynamics methods. *J. Chem. Phys.* **81**, 511 (1984).
39. Frisch M. J. et al. *Gaussian 16* Revision A.03 (Gaussian, Inc., 2016).
40. Canneaux, S., Bohr, F. & Hénon, E. KiSTheP: a program to predict thermodynamic properties and rate constants from quantum chemistry results. *J. Comp. Chem.* **35**, 82–93 (2014).
41. Weigend, F. & Ahlrichs, R. Balanced basis sets of split valence, triple zeta valence and quadruple zeta valence quality for H to Rn: Design and assessment of accuracy. *Phys. Chem. Chem. Phys.* **7**, 3297–3305 (2005).
42. Armentrout, P. B. et al. Infrared multiple-photon dissociation spectroscopy of cationized glycine: effects of alkali metal cation size on gas-phase conformation. *Phys. Chem. Chem. Phys.* **24**, 22950–22959 (2022).
43. Grimme, S., Antony, J., Ehrlich, S. & Krieg, H. A consistent and accurate ab initio parametrization of density functional dispersion correction (DFT-D) for the 94 elements H–Pu. *J. Chem. Phys.* **132**, 154104 (2010).
44. Stanton, J. F. Why CCSD(T) works: a different perspective. *Chem. Phys. Lett.* **281**, 130–134 (1997).
45. Zhang, J. & Valeev, E. F. Prediction of reaction barriers and thermochemical properties with explicitly correlated coupled-cluster methods: a basis set assessment. *J. Chem. Theory Comput.* **8**, 3175–3186 (2012).
46. Galano, A., Alvarez-Idaboy, J. R., Ruiz-Santoyo, M. E. & Vivier-Bunge, A. Mechanism and kinetics of the reaction of OH radicals with glyoxal and methylglyoxal: a quantum chemistry+CVT/SCT approach. *ChemPhysChem* **5**, 1379–1388 (2004).
47. CHEMKIN-PRO. *Reaction Design* (CHEMKIN-PRO, 2018).

Acknowledgements

This work is supported by the Advanced Materials-National Science and Technology Major Project (Grant No. 2024ZD0607000) and the National Natural Science Foundation of China (Grant No. 12302432).

Author contributions

T.Z.: Investigation, Writing—Original Draft, Writing—Review & Editing, Visualization, Methodology and Experiment; L.C.: Writing—Original Draft, Supervision and Resources; K.Y.: Investigation and Experiment; B.Z.: Investigation and Experiment; T.Y.: Investigation; Y.L.: Investigation and Methodology; J.L.: Investigation and Writing—Original Draft; D.L.: Investigation, Resources, Formal analysis, Writing—Original Draft and Writing—Review & Editing; J.C.: Supervision, Resources, Writing—Original Draft, Writing—Review & Editing, Methodology and Software.

Competing interests

The authors declare that they have no known competing financial interests or personal relationships that could have appeared to influence the work reported in this paper.

Additional information

Supplementary information The online version contains supplementary material available at <https://doi.org/10.1038/s42004-025-01582-3>.

Correspondence and requests for materials should be addressed to Lang Chen, Danyang Liu or Jun Chen.

Peer review information *Communications Chemistry* thanks the anonymous reviewers for their contribution to the peer review of this work.

Reprints and permissions information is available at <http://www.nature.com/reprints>

Publisher's note Springer Nature remains neutral with regard to jurisdictional claims in published maps and institutional affiliations.

Open Access This article is licensed under a Creative Commons Attribution-NonCommercial-NoDerivatives 4.0 International License, which permits any non-commercial use, sharing, distribution and reproduction in any medium or format, as long as you give appropriate credit to the original author(s) and the source, provide a link to the Creative Commons licence, and indicate if you modified the licensed material. You do not have permission under this licence to share adapted material derived from this article or parts of it. The images or other third party material in this article are included in the article's Creative Commons licence, unless indicated otherwise in a credit line to the material. If material is not included in the article's Creative Commons licence and your intended use is not permitted by statutory regulation or exceeds the permitted use, you will need to obtain permission directly from the copyright holder. To view a copy of this licence, visit <http://creativecommons.org/licenses/by-nc-nd/4.0/>.

© The Author(s) 2025